Redox- and metal-directed structural diversification in designed metalloprotein assemblies

Albert Kakkis[a], Eyal Golub[a], Tae Su Choi[a], and F. Akif Tezcan[a]

[a]Department of Chemistry and Biochemistry, University of California, San Diego, La Jolla, California, 92093

Supporting Materials, Tables, and Figures

Materials and Methods

Mutagenesis, Expression, and Purification. $^{A74/C96}$RIDC1 is a variant of Rosetta interface design cytochrome-1 (RIDC1), which is itself a variant of cytochrome cb_{562}.[1] PCR-based site-directed mutagenesis of plasmids encoding RIDC1 (pET20b-[RIDC1]) was performed as previously described.[2] Purified plasmids were transformed into competent BL21 (DE3) *E.coli* cells containing the *ccm* (cytochrome c maturation) cassette plasmid, pEC86.[3] Colonies were allowed to grow for 20 hours on LB/agar plates containing ampicillin (100 µg/mL) and chloramphenicol (34 µg/mL). Starter cultures were grown overnight for 16 hours at 37°C in LB media supplemented with the same antibiotic concentrations, diluted 100-fold into fresh, antibiotic supplemented LB media, and then grown at 37°C until the OD_{600} reached 0.6-1. Cultures were inoculated into 2.8 L glass flasks containing 1 L of LB media supplemented with antibiotics and shaken at 100 RPM for 20-24 hours at 37°C. Cells were pelleted via centrifugation (5,000 x g, 4°C, 5 min) and the media discarded. The red cell pellets were resuspended in a 10 mM sodium acetate buffer solution (pH 5.0) and vigorously stirred until all pellets were resuspended. The resulting mixture was sonicated for 15 min in pulses of 30 s on and 60 s off (Qsonica). The lysate was titrated with sodium hydroxide to a pH of 10, and then acetic acid to a pH of 5.0, and then clarified by centrifugation (10,000 x g, 4°C, 20 min). The cleared lysate was applied to a CM Sepharose Fast Flow (Biorad) resin preequilibrated with a 10 mM sodium acetate buffer solution (pH 5.0) and eluted using a step-gradient of 0-500 mM NaCl. The visibly red eluate was pooled, concentrated, and exchanged into 10 mM NaP_i buffer solution (pH 8.0). The protein was then loaded onto a 5 mL High-Q cartridge column preequilibrated with the same buffer solution and eluted using a step-gradient of 0-1 M NaCl. Fractions with Reinheitszahl ratios (A_{415}/A_{280}) above 3 were pooled, concentrated, exchanged into a 20 mM MOPS buffer solution supplemented with 150 mM NaCl, and loaded onto a Superdex S75 size column. Fractions with Reinheitszahl ratios (A_{415}/A_{280}) above 5.5 were pooled, concentrated, and treated with 5 mM EDTA/DPA.

Sedimentation velocity analytical ultracentrifugation (SV-AUC). Oxidized protein samples (200 µM monomer) were mixed directly with metal salts. To obtain reduced protein samples (200 µM monomer), the samples were incubated with 5 equivalents Tris(3-hydroxypropyl) phosphine (THPP) for 15 minutes prior to metal addition. Co^{II}, Ni^{II}, Cu^{II}, and Zn^{II} additions were made at 1 equivalent metal/monomer under aerobic conditions, while Fe^{II} additions were made at 1 or 5 equivalents/monomer in an anaerobic chamber. Due to the possibility of irreversible electron transfer from non-heme Fe^{II} to the ferric-heme cofactors of $^{A74/C96}$RIDC1 under oxidized conditions, SV measurements of $^{A74/C96}$RIDC1^{ox} mixed with Fe^{II} are not reported. Sedimentation velocity (SV) measurements were made in a solution of 20 mM TRIS (pH 7.5) at 25°C on a Beckman XL-A instrument equipped with a AN-60 Ti rotor and at 41,000 RPM. Samples were monitored at 570 nm (corresponding to a Q band of cytochrome) up to 12 h. Scans were processed and molecular weight distributions calculated using SEDFIT software.[4] Fitting parameters such as the buffer density (0.9988 g/mL), buffer viscosity (0.01007 poise), and partial specific volume (0.7313 mL/g) were calculated by SEDNTERP. SV profiles are shown at a confidence level of 95%.[4, 5] Oligomerization yields were estimated based on Riemann integrations of the peaks of the SV profiles, where the bounds of each discrete peak were defined by the full width at half maximum (FWHM).

X-ray Structure Determination. Crystals of $^{A74/C96}$RIDC1 variants were obtained by sitting-drop vapor diffusion at 25°C. To obtain crystals of oxidized samples, 2-2.5 mM protein monomer was mixed with 1-5 equivalents of metal salts for at least one hour at 25°C. To obtain crystals of reduced samples, 2-2.5 mM protein monomer was mixed with 5-10 equivalents of either THPP or tris(2-carboxyethyl)phosphine (TCEP) prior to metal addition in an anaerobic chamber. Metal-loaded samples were mixed at a ratio of 1 µL: 1 µL or 2 µL: 1 µL with mother liquor. All crystals

were transferred into perfluoro polyether (Hampton) for cryoprotection prior to freezing. Diffraction data were collected at 80-100 K on ALS Beamline 5.0.1 (Apo [$^{A74/C96}$RIDC1^{ox}]$_4$), SSRL Beamline 9-2 (Co_2:[$^{A74/C96}$RIDC1^{ox}]$_4$, Zn_2:[$^{A74/C96}$RIDC1^{ox}]$_4$, Fe_2: [$^{A74/C96}$RIDC1^{red}$_3$], Ni_2: [$^{A74/C96}$RIDC1^{red}]$_3$, Zn_4: [$^{A74/C96}$RIDC1^{red}]$_4$), and ALS Beamline 8.3.1 (Cu_4: [$^{A74/C96}$RIDC1^{red}]$_4$). Diffraction data were processed using either iMOSFLM or XDS and scaled using SCALA.[6] Molecular replacement was carried out using Phaser with monomeric cytochrome cb_{562} (PDB: 2BC5) as the search model.[7] Refinement was performed using phenix.refine while model building and placement of metal ions/water was performed using COOT.[8] Electron density maps were generated using Phenix and then converted into CCP4 map files using a Fast Fourier Transform algorithm (FFT, CCP4i).[6] All final models and CCP4 electron density maps were rendered in PYMOL (www.pymol.org). Surface calculations were performed using PISA.[9]

Rosetta Interface Energy Calculations: To estimate the stability of Fe_2:[$^{A74/C96}$RIDC1^{red}]$_3$ and Ni_2:[$^{A74/C96}$RIDC1^{red}]$_3$ based on non-covalent interactions while excluding the contribution of metal-ligand interactions, Rosetta score calculations were performed on Fe_2:$^{A74/C96}$RIDC1^{red}$_3$ and Ni_2:$^{A74/C96}$RIDC1^{red}$_3$ crystal structures. In each case, the heme cofactors and all metal ions and water molecules were removed prior to loading the trimeric complex into Rosetta. After evaluating the Rosetta score of the trimer, the chains were moved 100 Å apart and the Rosetta score of the system was re-evaluated. Following these calculations, the sum of REU values for metal-binding histidine residues (H59, H63, H73, H77) was subtracted from each Rosetta score. Finally, the adjusted Rosetta score of the trimer was subtracted from that of the separated chains to obtain a ΔREU value that serves as a proxy for the $\Delta\Delta$G of trimerization.[10]

DFT calculations: All metal complexes were extracted from crystal structures of RIDC1 variants. Input files were prepared using Avogadro software.[11] Single point calculations were performed at the level of B3LYP theory using the 6-31G basis set.[12] Calculations were performed without an initial geometry optimization step to avoid introducing model bias. To generate the hypothetical Ni^{II}:His_6 coordination site in Fe_2: [$^{A74/C96}$RIDC1^{red}$_3$], the position of the His77 residue of the Fe^{II}:His_5 site was modified to be within coordinating distance of the metal center. This new rotamer was predicted by the Dunbrack rotamer library to be the most stable metal-binding rotamer accessible.[13]

Supplementary Discussion

Oligomerization of metal-directed $^{A74/C96}$RIDC1^{red} assemblies. As described in the main text, the addition of Fe^{II} or Ni^{II} to $^{A74/C96}$RIDC1^{red} gives rise to two structurally distinct trimers: an "up-up-down" trimer (+Fe^{II}) and an "up-up-up" trimer (+Ni^{II}). The "up-up-down" trimer hosts His_3 and His_5 coordination sites in a square pyramidal geometry while the "up-up-up" trimer hosts His_6 sites in an octahedral geometry. According to crystal field theory, the crystal field stabilization energy (CFSE) of Ni^{II} in an octahedral coordination environment is higher than that of Fe^{II}. Correspondingly, our DFT calculations predict that altering the coordination environment in Ni^{II} coordination complexes from square pyramidal His_3/His_5 to octahedral His_6 imparts greater stability than it does in Fe^{II} complexes (**Figure S13, Table S6**). Based on crystal field theory and DFT calculations, we surmise that Ni^{II} is more likely than Fe^{II} to direct protein assembly into an architecture that features octahedral His_6 coordination sites. Rotamer analysis of the His_5 coordination site of the "up-up-down" trimer reveals that the most probable metal coordinating rotamer of H77'' gives rise to a His_6 environment that is more geometrically distorted than that of the "up-up-up" trimer (**Figure S14**). Correspondingly, this hypothetical site is predicted by DFT to be less thermodynamically stable by 116 kcal/mol (**Figure S14b-c, Table S6**). This result suggests that the "up-up-down" trimer, which hosts the Fe^{II} coordination sites, is less effective at templating octahedral His_6 sites than the "up-up-up" trimer.

Interestingly, the "up-up-down" trimer is predicted by Rosetta calculations to be a more stable trimer based purely on non-covalent interactions (**Table S1, S5**). We can thus surmise that in the case of Ni^{II}-directed assembly, the thermodynamic stabilization of the metal ion in an octahedral, His_6 coordination environment–which would bias trimerization into the "up-up-up" conformation–is greater than the thermodynamic stabilization provided by additional non-covalent interactions present in the "up-up-down" conformation. In the case of Fe^{II}-directed assembly, the inverse is true.

In contrast to the Fe^{II}- and Ni^{II}-directed assemblies, the Zn^{II}-directed assembly is a tetramer hosting four identical, tetrahedral His_2GluCys coordination sites. According to the MetalPDB, 40% of natural Zn^{II} metalloproteins feature coordinatively saturated, tetrahedral coordination sites.[14] By contrast, the frequencies of octahedral and square pyramidal geometries are only 7%.[14] Among coordinatively saturated, tetrahedral Zn^{II} sites, 67% feature at least one cysteine in the primary sphere.[14] The bioinformatic data suggests that a tetrahedral His_2GluCys primary sphere would be highly favorable for Zn^{II} coordination. We also have observed tetrahedral Zn^{II} coordination in many of our designed tetrameric assemblies, including Zn_4:MBPC1$_4$ and Zn_4:RIDC1$_4$.[15, 16]

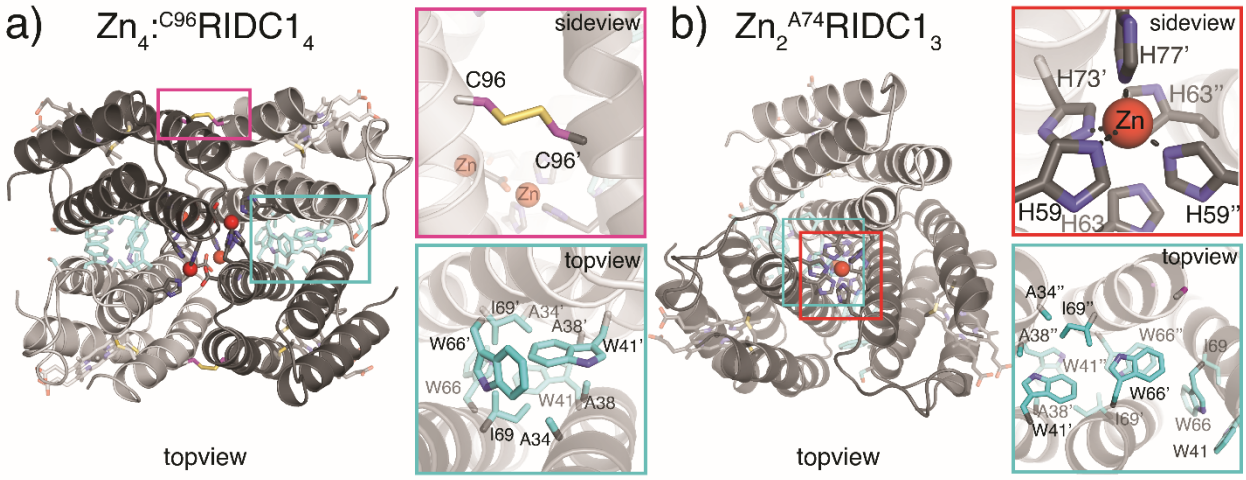

Figure S1. (a) Crystal structure of Zn_4:^{C96}RIDC1$^{ox}_4$ (PDB ID: 3IQ6). One of the two C96-C96 disulphide bonds is highlighted in magenta while the designed hydrophobic residues are highlighted in cyan. (b) Crystal structure of Zn_2:^{A74}RIDC1$_3$ (PDB ID: 3M15). One of the two Zn:His_4 coordination sites is highlighted in red while the designed hydrophobic residues are highlighted in cyan. ^{C96}RIDC1 enforces the tetrameric architecture through covalent preorganization of the *i1* interface while ^{A74}RIDC1 features a decoupling of Zn binding to tetramerization. This decoupling takes place despite the presence of hydrophobic residues installed to stabilize a tetramer, which suggests that Zn coordination by D74 plays a valuable role in directing the tetramerization of RIDC1.

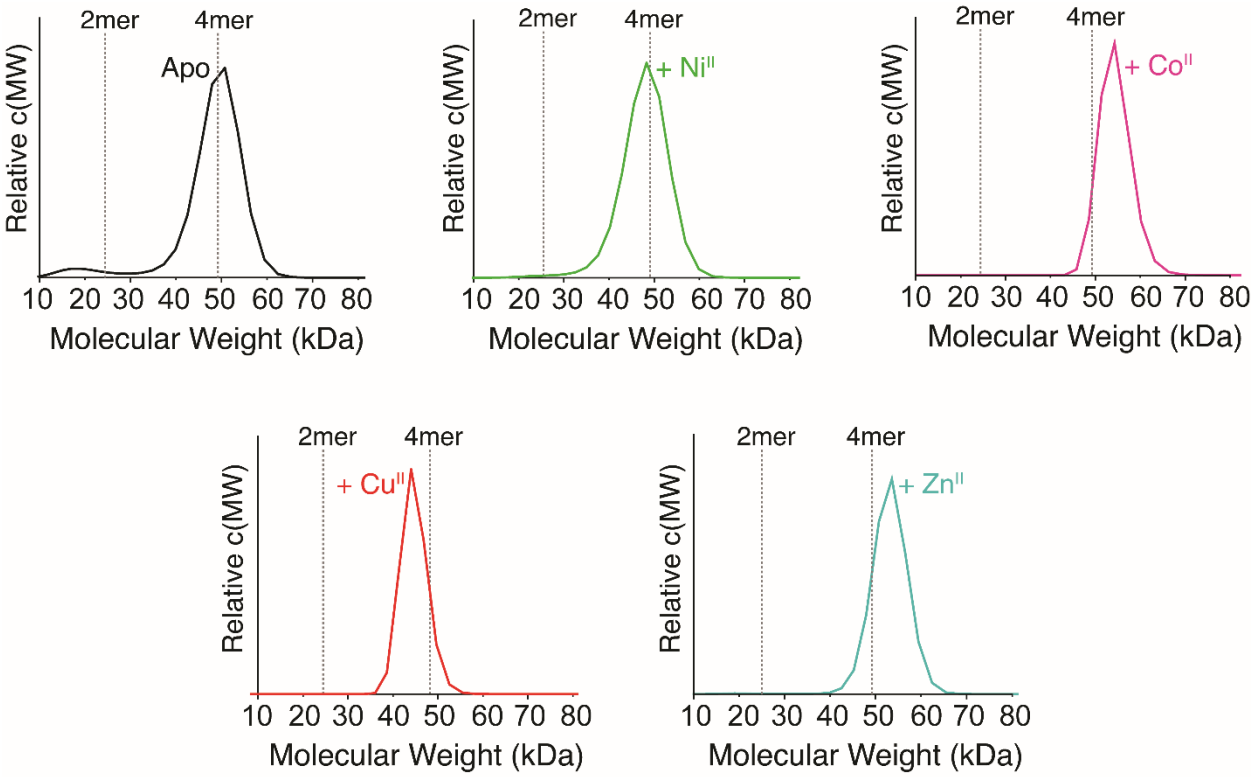

Figure S2. SV-AUC distributions of metal-supplemented $^{A74/C96}$RIDC1^{ox}. Analysis was performed with 200 μM protein monomer and 1 equivalent metal salt.

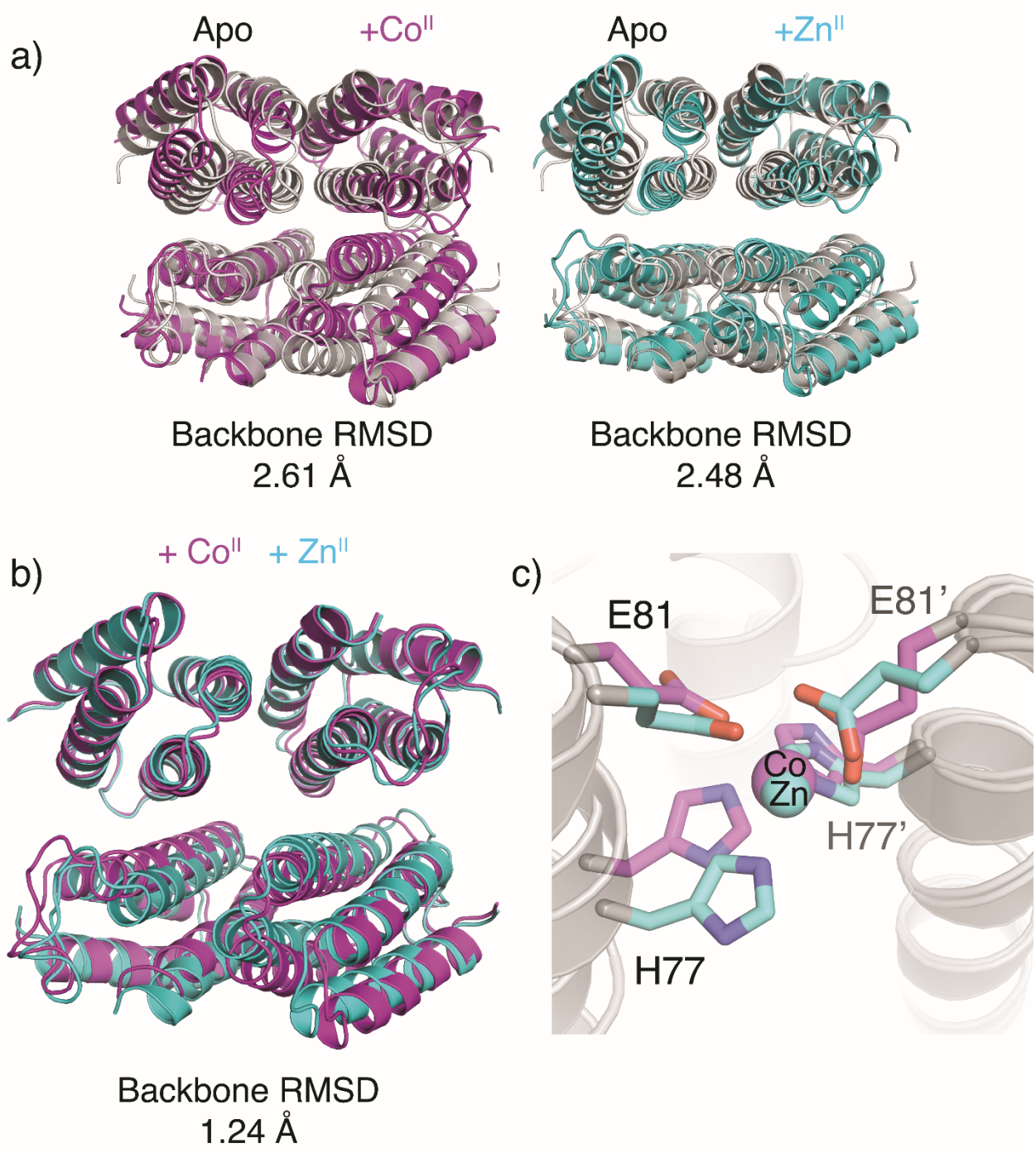

Figure S3. (a) Overlays of Apo, Co^{II}-, and Zn^{II}-bound $^{A74/C96}$RIDC1^{ox} crystal structures (b) Overlay of Co^{II}-, and Zn^{II}-bound $^{A74/C96}$RIDC1^{ox} crystal structures. (c) Overlay of C_2 coordination sites of the metal-loaded assemblies, illustrating close correlation in the positions of coordinating residues.

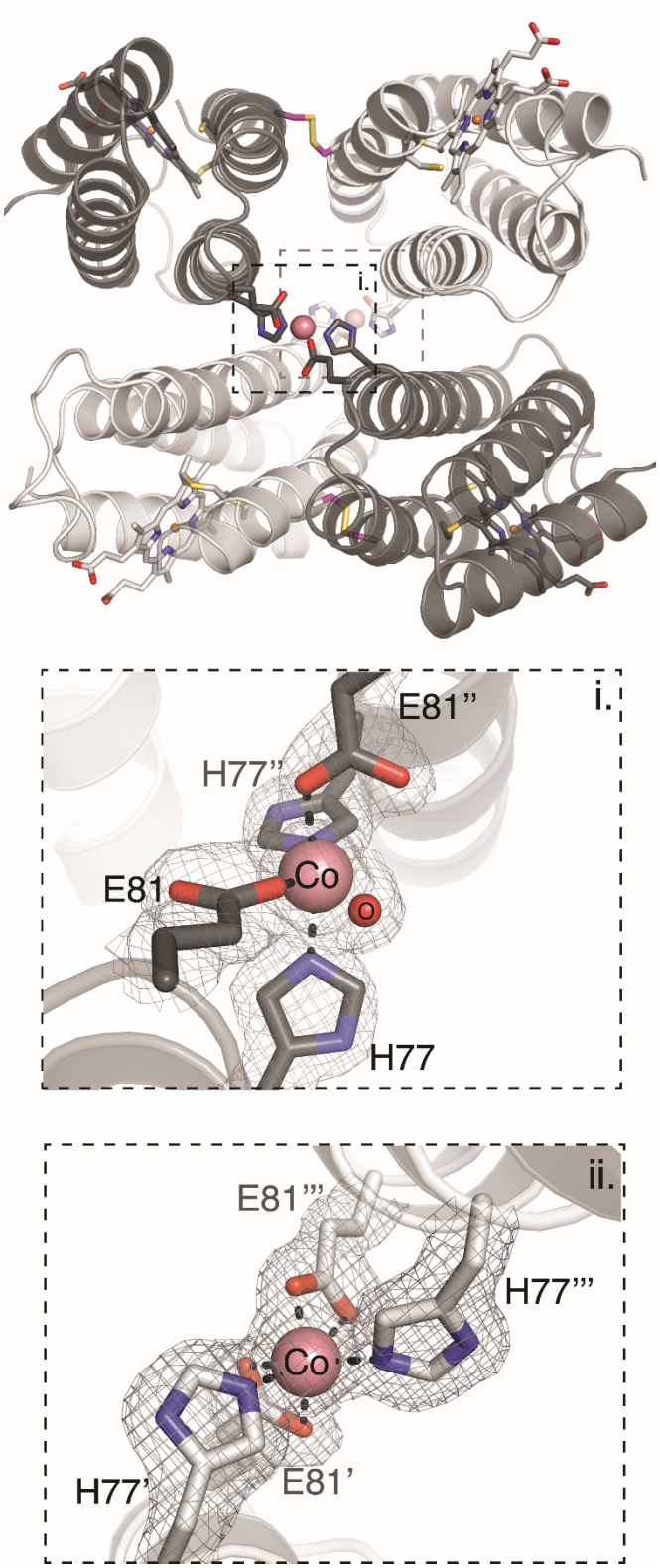

Figure S4. Overview of Co_2:[$^{A74/C96}$RIDC1^{ox}]$_4$ crystal structure, including 2Fo-2Fc maps of metal coordination sites. All electron density maps were generated in CCP4i.

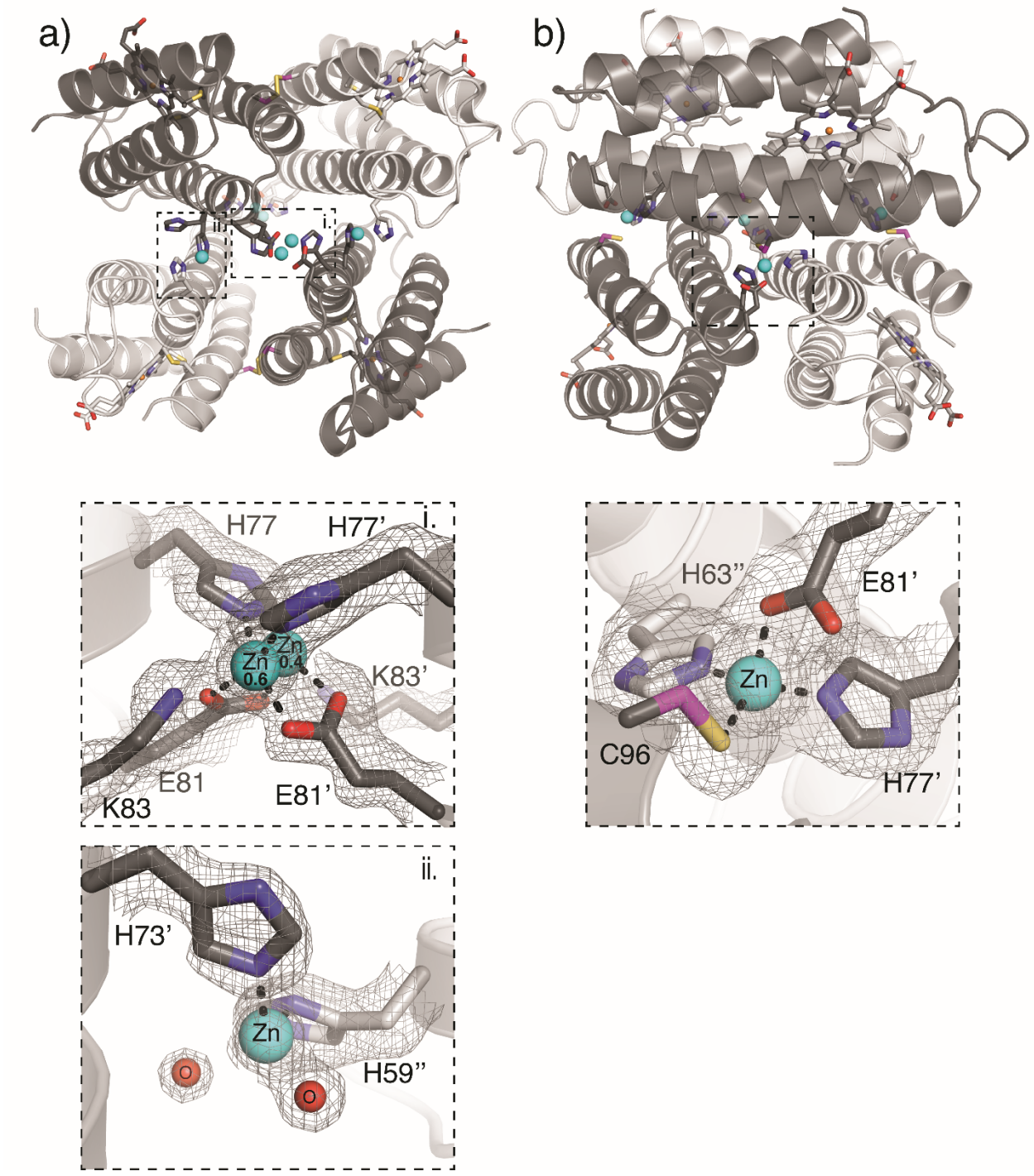

Figure S5. Overviews of (a) Zn_4:[$^{A74/C96}$RIDC1^{ox}]$_4$ and (b) Zn_4:[$^{A74/C96}$RIDC1^{red}]$_4$ crystal structures, including 2Fo-2Fc maps of metal coordination sites. At the first coordination site of Zn_4:$^{A74/C96}$RIDC1$^{ox}{}_4$ (i), a single Zn ion occupies two discrete positions (occupancies in bold). K83 residues form close contacts (2.5 Å) with Zn, but this interaction cannot be unequivocally characterized as metal-ligand coordination and the pKa of K83 is unknown.

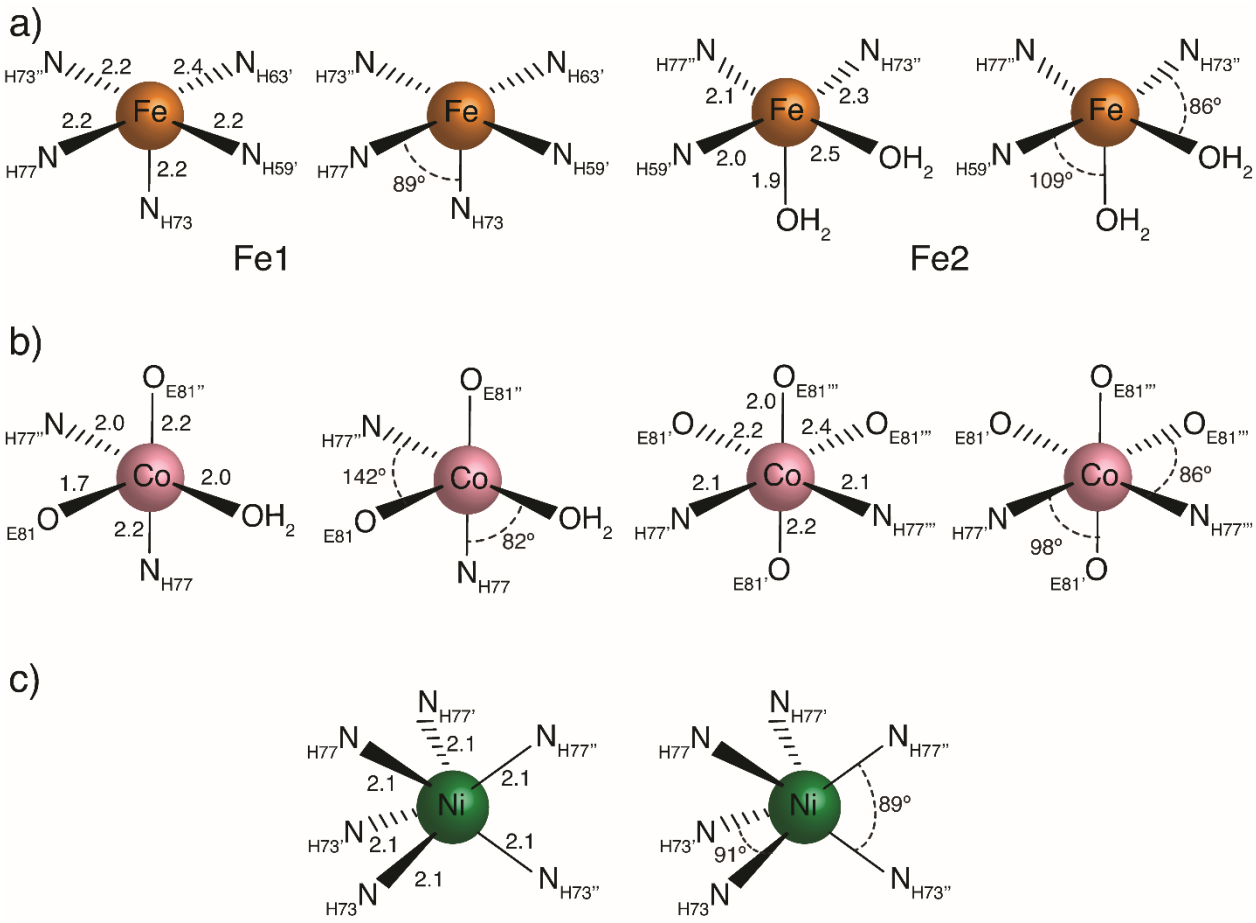

Figure S6. Geometries of coordination sites in (a) Fe_2:[$^{A74/C96}$RIDC1^{red}]$_3$, (b) Co_2:[$^{A74/C96}$RIDC1^{ox}]$_4$, and (c) Ni_2:[$^{A74/C96}$RIDC1^{red}]$_3$, including bond distances and angles. Significant distortions from ideal coordination geometries are observed in all metal-bound structures other than Ni_2:[$^{A74/C96}$RIDC1^{red}]$_3$.

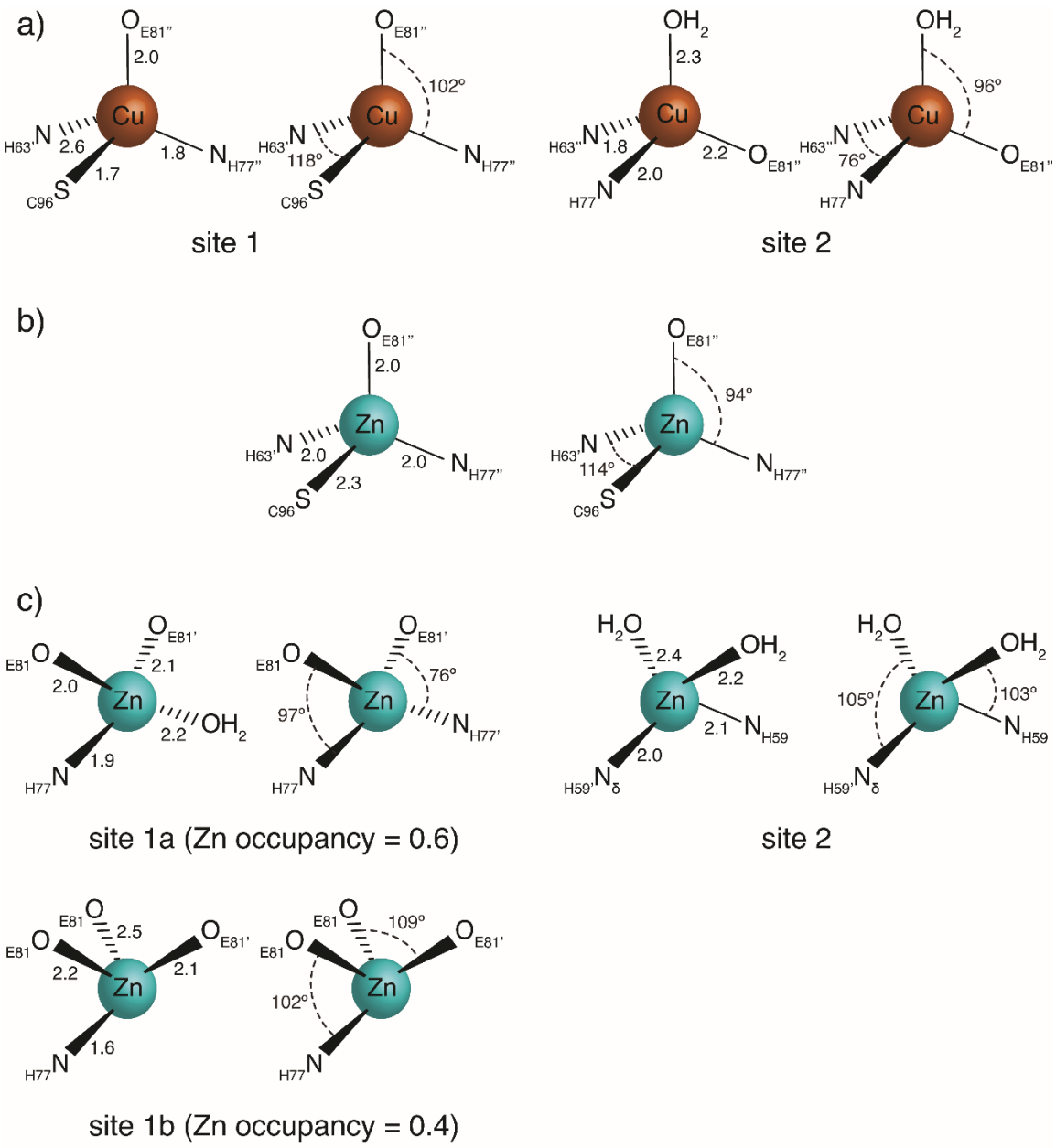

Figure S7. Geometries of coordination sites in (a) Cu_4:[$^{A74/C96}$RIDC1^{red}]$_4$, (b) Zn_4:[$^{A74/C96}$RIDC1^{red}]$_4$, and (c) Zn_4:[$^{A74/C96}$RIDC1^{ox}]$_4$, including bond distances and angles.

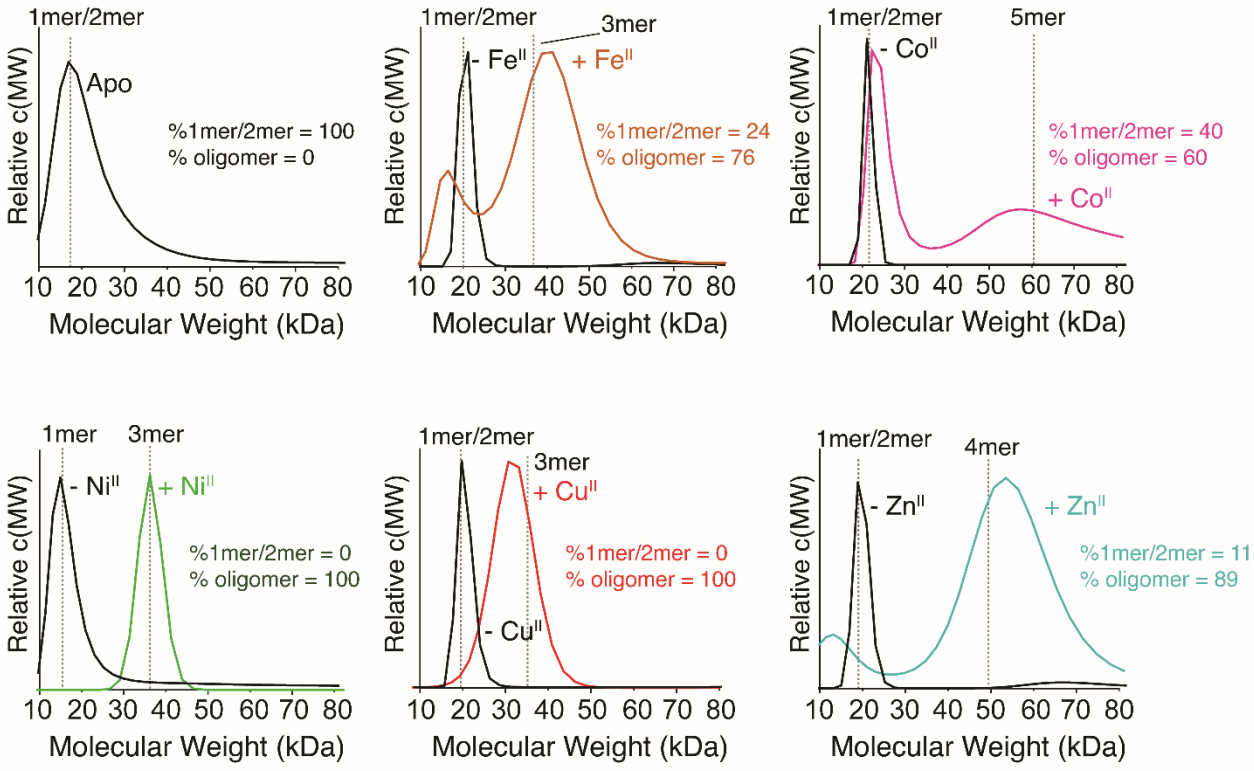

Figure S8. SV-AUC distributions of $^{A74/C96}$RIDC1^{red} upon the addition/removal of metal ions. Analysis was performed with 200 μM protein monomer and 1 equivalent (Co^{II}, Ni^{II}, Cu^{II}, Zn^{II}) or 5 equivalents (Fe^{II}) metal salt. Metal ions were removed from the protein via the addition of 10 mM EDTA/DPA (black traces).

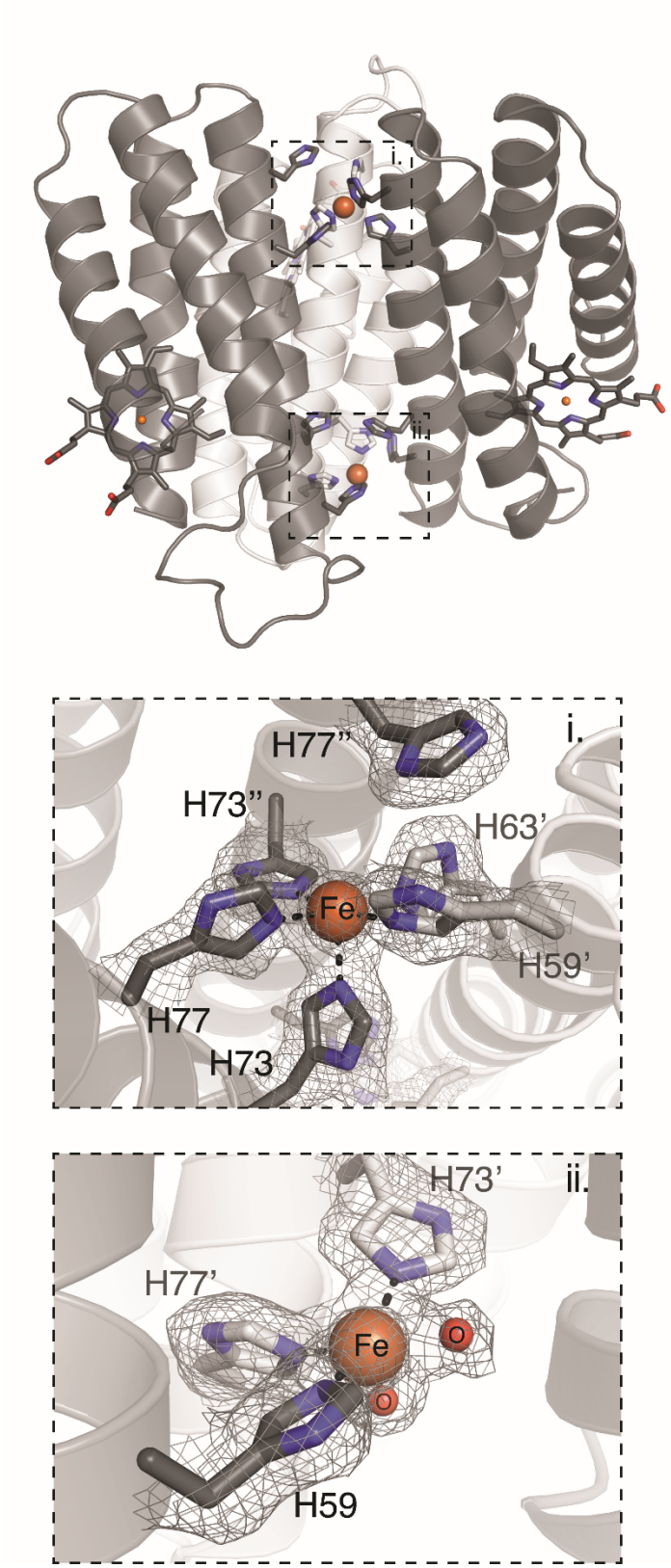

Figure S9. Overview of Fe_2:[$^{A74/C96}$RIDC1^{red}]$_3$ crystal structure, including 2Fo-2Fc maps of metal coordination sites. All electron density maps were generated in CCP4i.

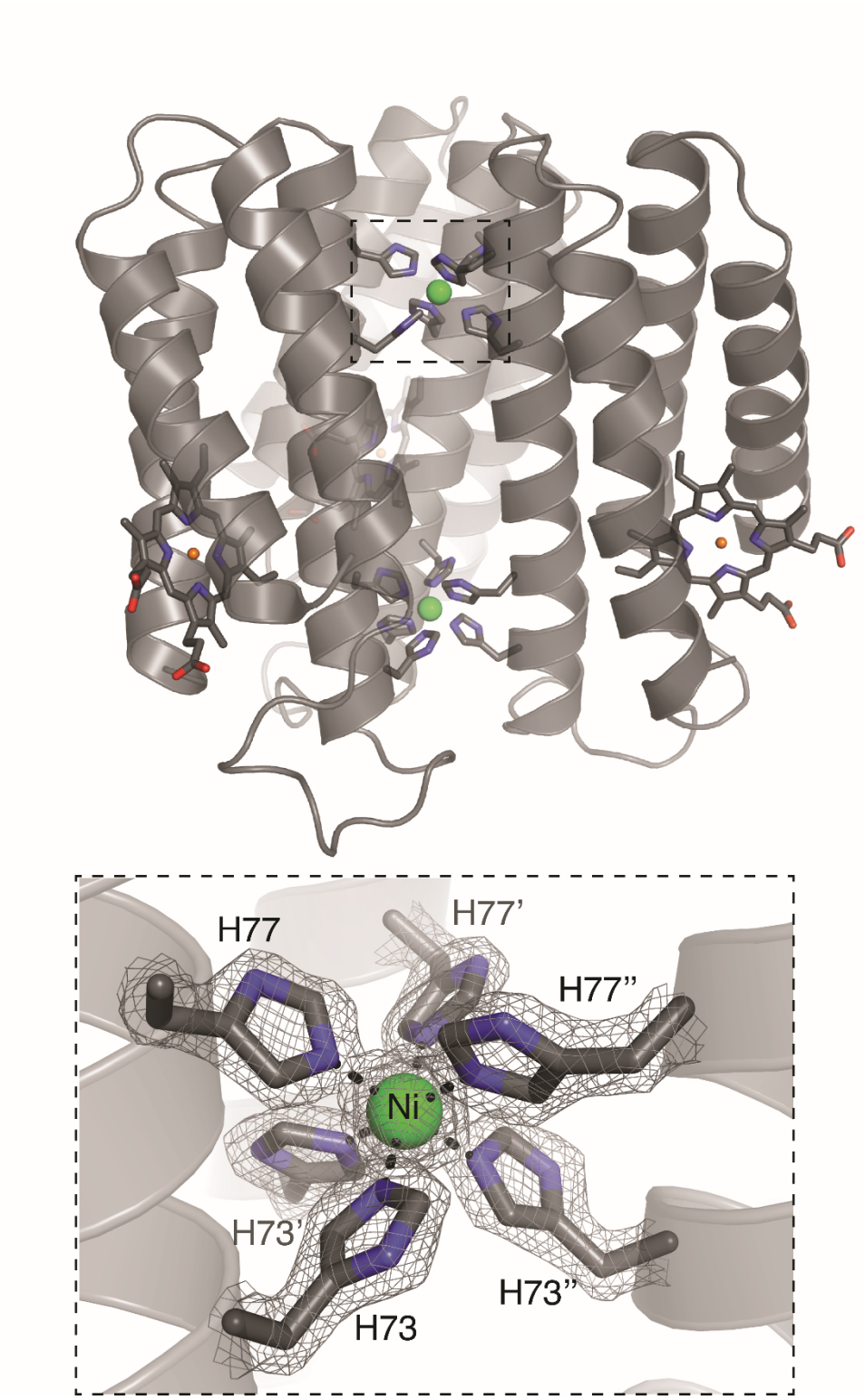

Figure S10. Overview of the Ni_2:[$^{A74/C96}$RIDC1^{red}]$_3$ crystal structure, including a 2Fo-2Fc map of one of the Ni:His_6 coordination sites. In accordance with the C_3 symmetry of the assembly, the coordination sites are identical in terms of bond distances and angles.

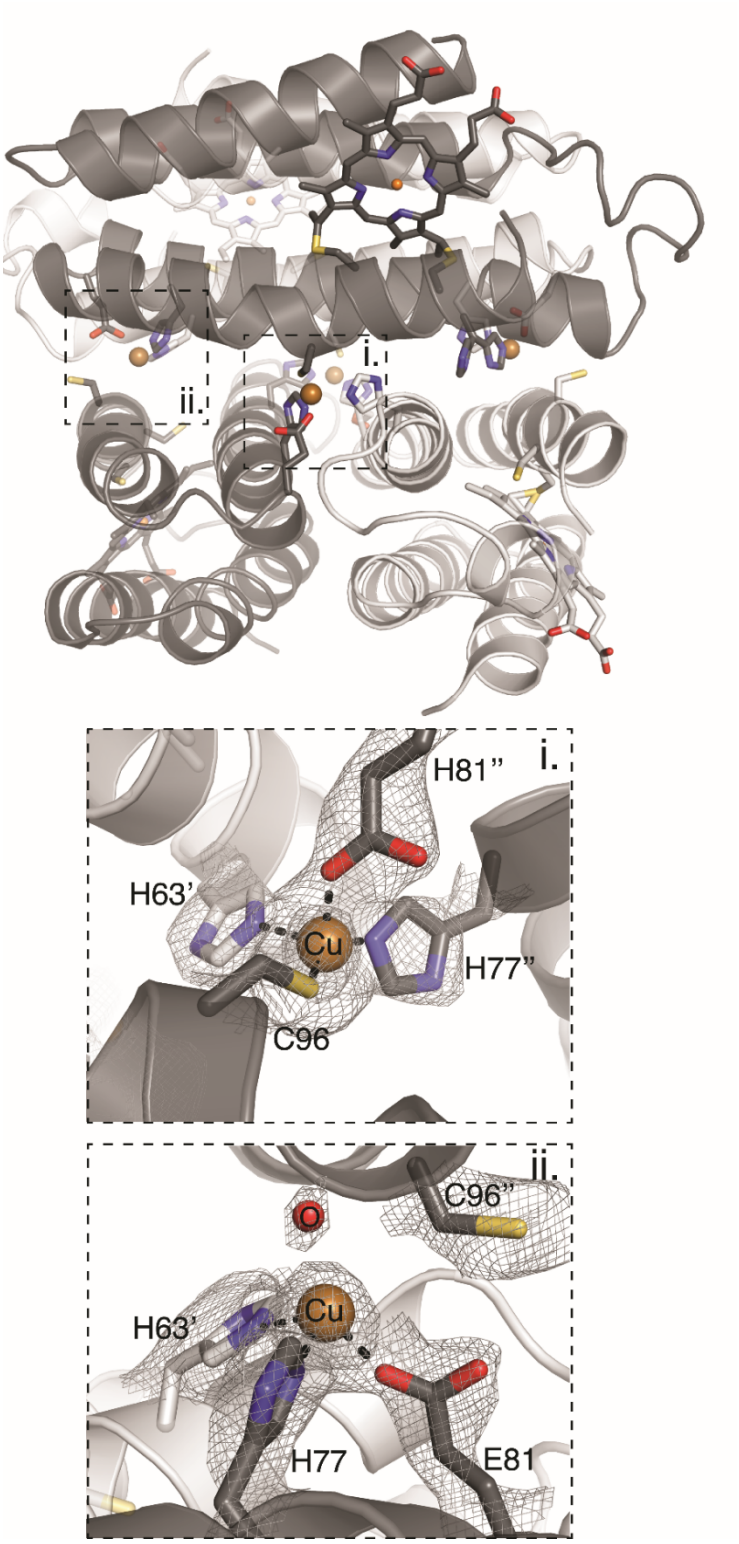

Figure S11. Overview of the Cu_4:[$^{A74/C96}$RIDC1^{red}]$_4$ crystal structure, including 2Fo-2Fc maps of metal coordination sites. The tetrahedral coordination geometry of the Cu ions suggests *in situ* reduction of copper ions by THPP to Cu^{I}, which is more frequently observed in these coordination environments.

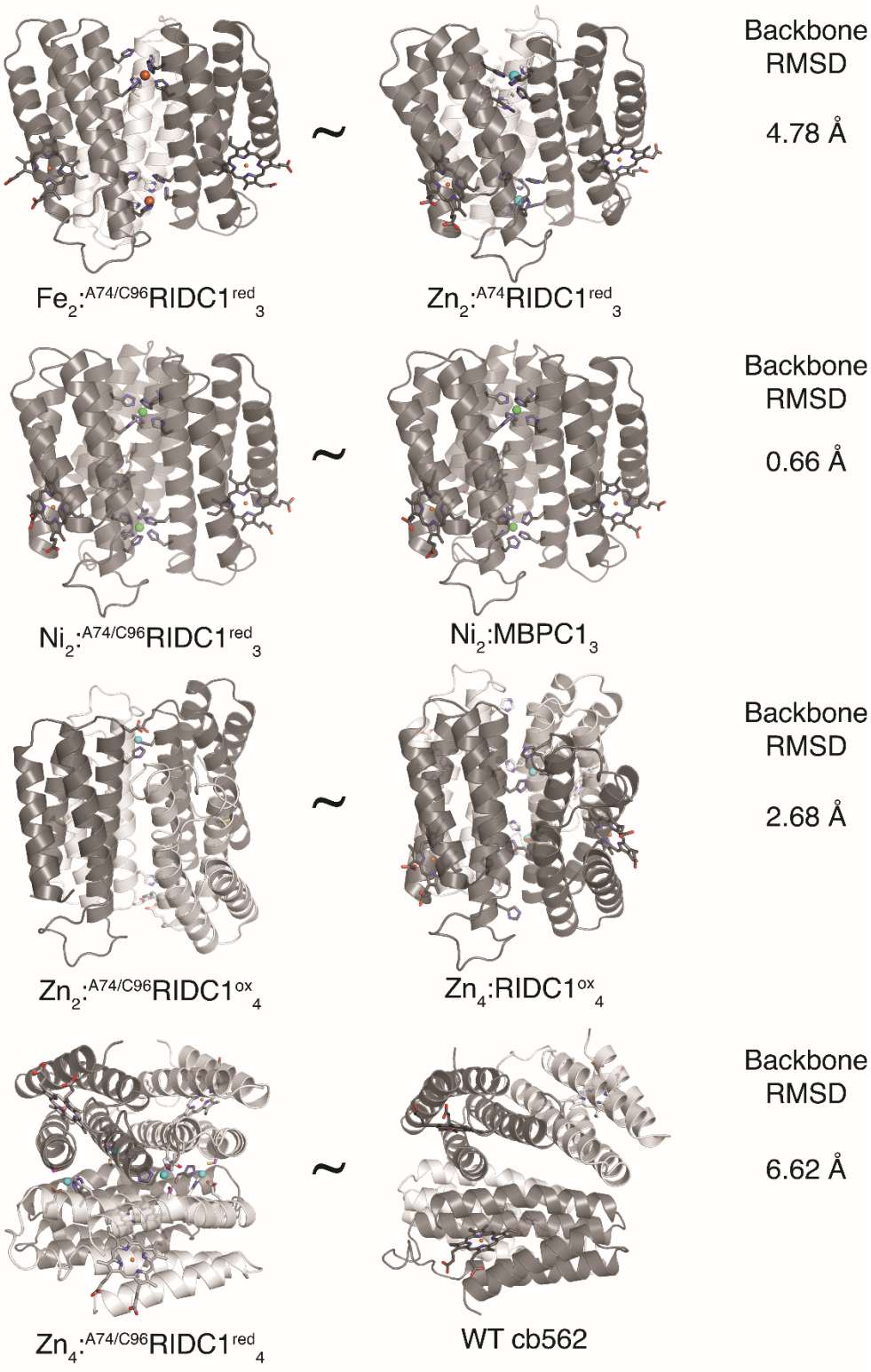

Figure S12. Comparison of metal-bound $^{A74/C96}$RIDC1^{red} structures with other cytochrome *cb*562 variants. Sequence-independent alignments were carried out in PYMOL.

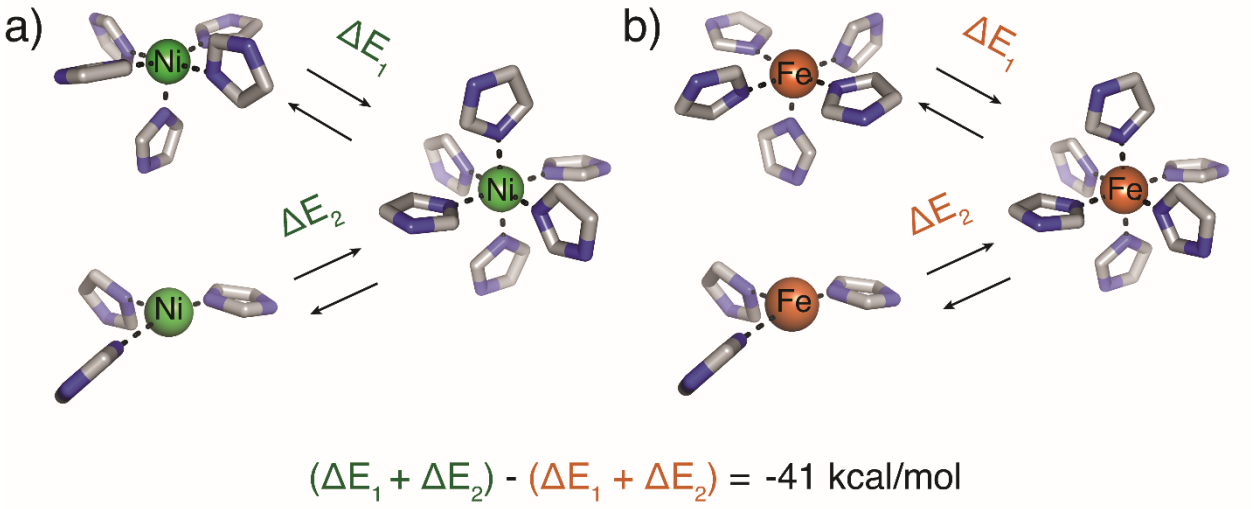

Figure S13: DFT calculations on the relative stability of His_3, His_5, and His_6 coordination environments at (a) Ni^{II} and (b) Fe^{II} centres. Prior to the calculations, Ni^{II} was substituted into the Fe:His_3 and Fe:His_5 coordination sites extracted from the Fe_2: $[^{A74/C96}RIDC1^{red}]_3$ crystal structure, while Fe^{II} was substituted into one of the Ni^{II}:His_6 coordination sites extracted from the Ni_2: $[^{A74/C96}RIDC1^{red}]_3$ crystal structure. Calculations were performed without geometry optimization. The calculations predict that Ni^{II} is more stabilized by His_6 coordination than Fe^{II}, by 41 kcal/mol. We surmise that the relative stabilization of Ni^{II} in a His_6 coordination environment is enough to bias trimerization in the “up-up-up” arrangement.

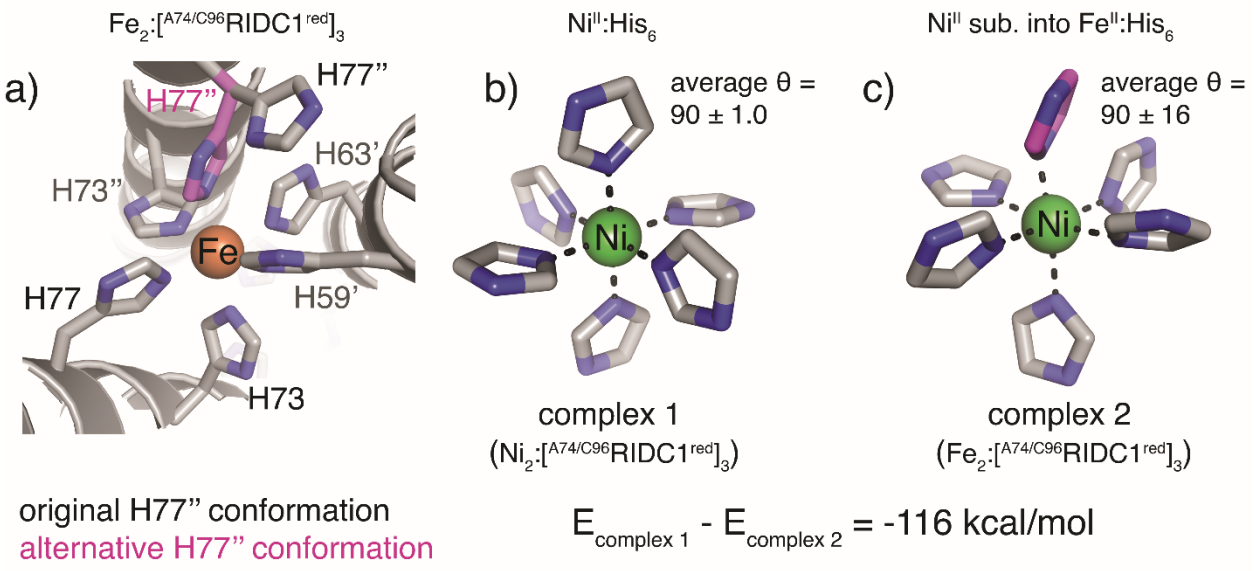

Figure S14: Modeling and DFT calculations of a hypothetical His_6 coordination site in Fe_2:[$^{A74/C96}$RIDC1^{red}]$_3$. (a) Overlay of coordination sites in the Fe^{II}-directed trimer with and without the alternative H77'' conformation that would give rise to a Fe^{II}:His_6 site. The alternative conformation of H77'' (magenta) represents the highest probability rotamer within coordinating distance of Fe^{II} as predicted by the Dunbrack rotamer library. (b) Model of Ni^{II}:His_6 in the Ni^{II}-directed trimer. (c) Model of the hypothetical Fe^{II}:His_6 site in Fe_2:[$^{A74/C96}$RIDC1^{red}]$_3$ substituted with Ni^{II}. Significant deviations from ideal bond angles of an octahedral coordination geometry were observed in the hypothetical site, which led to a lower DFT-computed energy.

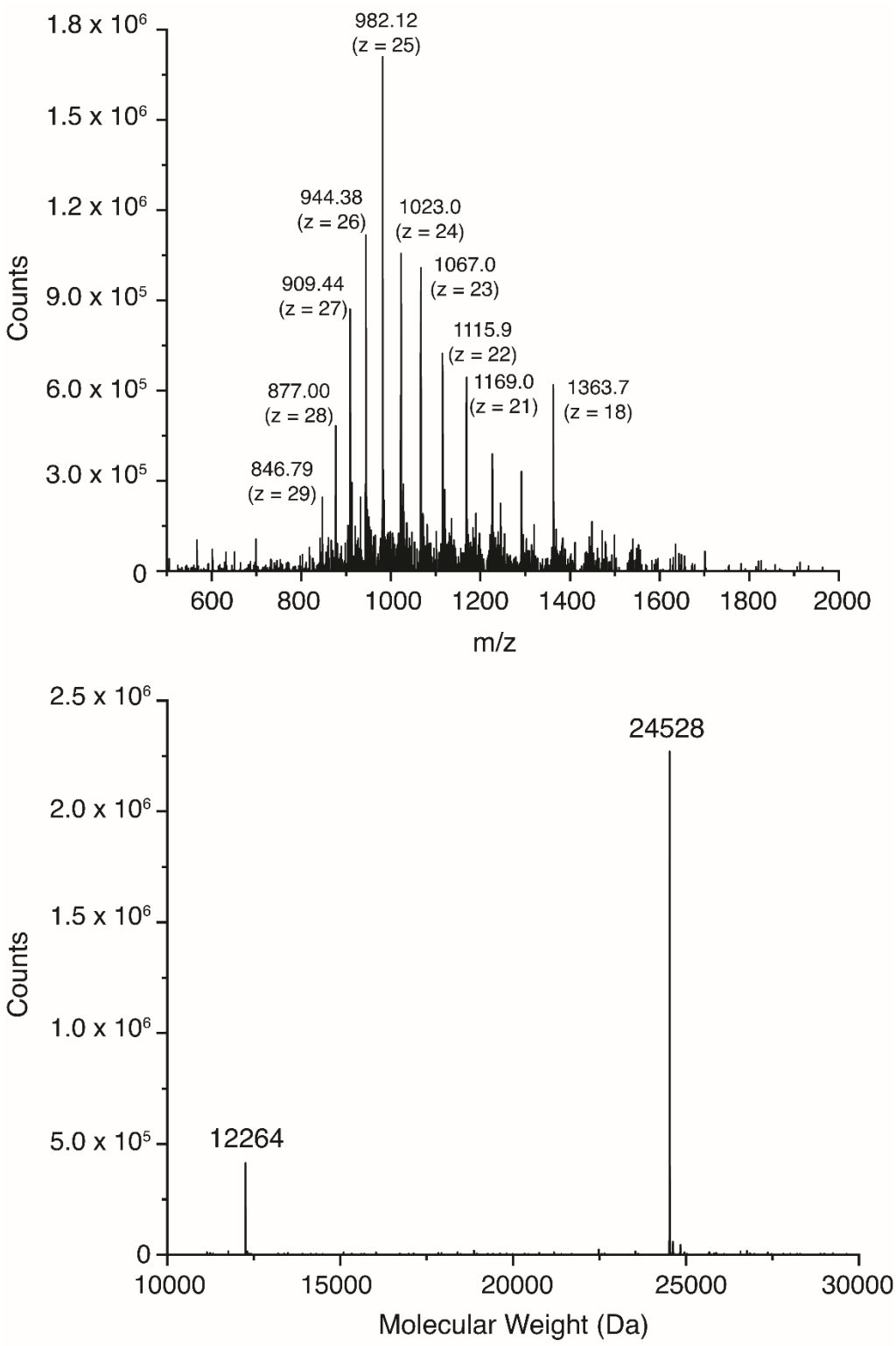

Figure S15. Convoluted (top) and deconvoluted (bottom) ESI-MS spectra of $^{A74/C96}$RIDC1^{ox}. Charge states and m/z values in the convoluted spectrum correspond to the dimer.

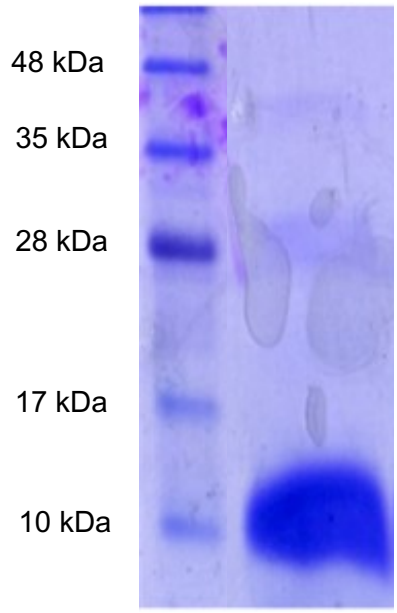

Figure S16. Denaturing SDS-PAGE gel of $^{A74/C96}$RIDC1. The gel was run at 200 V for 45 minutes and under reducing conditions.

Table S1. Buried surface area (BSA) calculations of RIDC1 assemblies[a]

Variant	Reductant	Metal	BSA/monomer (Å^2)
$^{A74/C96}$RIDC1	-	-	1665
$^{A74/C96}$RIDC1	-	Co	968
$^{A74/C96}$RIDC1	-	Zn	1068
$^{A74/C96}$RIDC1	THPP	Fe	1038
$^{A74/C96}$RIDC1	THPP	Ni	768
$^{A74/C96}$RIDC1	THPP	Cu	1743
$^{A74/C96}$RIDC1	THPP	Zn	1650
^{C96}RIDC1	-	-	1063
^{C96}RIDC1	-	Zn	1388
^{A74}RIDC1	-	Zn	1007

[a] BSA calculations based on crystal structures

Table S2. SV-AUC parameters for apo, metal-loaded $^{A74/C96}$RIDC1[a]

Reductant[b]	**Metal[c]**	**Frictional Ratio (f/f_0)**	**MW_{max} (kDa)[d]**
-	-	1.31	51
-	$CoCl_2$	1.20	54
-	$NiCl_2$	1.20	48
-	$CuCl_2$	1.21	44
-	$ZnCl_2$	1.12	54
THPP	-	1.20	17
THPP	$FeSO_4$[e]	1.37	41
THPP	$CoCl_2$	1.16	22
THPP	$NiCl_2$	1.21	33
THPP	$CuCl_2$	1.21	31
THPP	$ZnCl_2$	1.19	54

[a] [protein monomer] = 0.2 mM monomer

[b] [THPP] = 1 mM

[c] Unless otherwise indicated, [metal] = 0.2 mM

[d] Theoretical MW = 12258 (monomer), 24516 (dimer), 36774 (trimer), 49032 (tetramer)

[e] [$FeSO_4$] = 1 mM

Table S3. X-ray refinement statistics for $^{A74/C96}$RIDC1 crystal structures. Numbers in parentheses correspond to values in the highest resolution shell.

Variant	Apo $[^{A74/C96}RIDC1^{ox}]_4$	Co_2: $[^{A74/C96}RIDC1^{ox}]_4$	Zn_4: $[^{A74/C96}RIDC1^{ox}]_4$	Fe_2: $[^{A74/C96}RIDC1^{red}]_3$
PDB ID	7RWV	7SU2	7RWW	7RWY
Space group	*I*4	*P*2$_1$	*P*2$_1$	*P*2$_1$
Cell dimensions (Å)	92.58, 92.58, 91.26	47.88 90.02 52.04	47.79, 86.91, 49.18	52.55, 82.68, 74.14
Cell angles (°)	90.00, 90.00, 90.00	90.00 95.91 90.00	90.00, 109.16, 90.00	90.00, 95.22, 90.00
Resolution (Å)	46.29-2.20	37.00-2.00	35.96-1.70	44.65-2.20
No. unique reflections	19413	29302	40172	30358
R_{merge}	0.150 (0.544)	0.017 (0.059)	0.115 (0.752)	0.096 (0.374)
Multiplicity	2.5 (2.6)	2.0 (2.0)	14.8 (10.9)	3.9 (3.8)
CC½	0.984 (0.363)	1 (0.989)	0.996 (0.617)	0.992 (0.863)
< I / σ(I) >	3.7 (1.9)	26.7 (7.4)	11.7 (3.2)	8.0 (2.8)
Completeness (%)	98.0 (98.7)	98.4 (96.0)	99.9 (99.5)	99.1 (99.7)
Refinement				
R_{work}/R_{free}	0.1946/0.2520	0.1904/0.1915	0.1704/0.2020	0.2023/0.2592
B-factors (Å^2)	34.36	34.32	29.84	39.71
Protein	34.76	34.37	29.15	39.64
Ligand/ion	28.36	29.71	29.63	39.86
Solvent	32.76	37.65	39.39	41.08
R.m.s deviations				
Bond lengths (Å)	0.016	0.009	0.012	0.009
Bond angles (°)	1.871	1.150	1.123	1.159
Clashscore	16.87	7.63	10.23	19.73
Ramachandran plot (%)				
Favored	99.76	97.84	99.76	97.44
Outliers	0.00	0.00	0.00	0.16
Rotamer outliers (%)	0.00	2.60	0.29	1.99

Table S3 (continued). X-ray refinement statistics for $^{A74/C96}$RIDC1 crystal structures. Numbers in parentheses correspond to values in the highest resolution shell.

Variant	Ni_2: $[^{A74/C96}RIDC1^{red}]_3$	Cu_4: $[^{A74/C96}RIDC1^{red}]_4$	Zn_4: $[^{A74/C96}RIDC1^{red}]_4$
PDB ID	7RWU	7TEP	7RWX
Space group	$P4_132$	$P2_1$	R 3 2
Cell dimensions (Å)	94.26, 94.26, 94.26	47.08 80.57 49.44	111.65, 111.65, 148.33
Cell angles (°)	90.00, 90.00, 90.00	90.00 102.33, 90.00	90.00, 90.00, 120.00
Resolution (Å)	42.15-1.80	45.99-2.70	37.01-1.60
No. unique reflections	25101	9589	27879
R_{merge}	0.069 (0.191)	0.0571 (0.146)	0.055
Multiplicity	68.0 (68.5)	3.3 (3.3)	4.1 (3.7)
CC ½	1.000 (0.998)	0.998 (0.953)	0.995 (0.898)
< I / σ(I) >	58.1 (28.2)	16.66 (6.50)	8.5 (2.7)
Completeness (%)	100.0 (100.0)	95.9 (89.6)	96.2 (91.3)
Refinement			
R_{work}/R_{free}	0.1641/0.1892	0.2536/0.3385	0.2369/0.2897
B-factors (Å^2)	23.60	28.62	50.21
Protein	21.49	28.66	50.60
Ligand/ion	16.75	28.86	44.24
Solvent	36.29	26.39	49.03
R.m.s deviations			
Bond lengths (Å)	0.010	0.019	0.008
Bond angles (°)	0.994	1.960	1.006
Clashscore	15.07	51.51	10.12
Ramachandran plot (%)			
Favored	99.04	77.88	98.08
Outliers	0.00	6.75	0.00
Rotamer outliers (%)	0.00	10.5	4.22

Table S4. Crystallization conditions for apo, metal-loaded $^{A74/C96}$RIDC1

Reductant[a]	Metal	[Protein][b]	[Metal]	Mother liquor
-	-	2.6 mM	-	30% PEG400, 0.1 M HEPES pH 7.5, 0.2 M $MgCl_2$
-	$CoCl_2$	3.0 mM	3.0 mM	30% PEG400, 0.1 M HEPES pH 7.5, 0.2 M NaCl
-	$ZnCl_2$	2.6 mM	2.6 mM	45% MPD, 0.1 M HEPES pH 7.5, 0.2 M $MgCl_2$
THPP[a]	$FeSO_4$	2.8 mM	9.0 mM	40% PPG, 0.1 M Bis-Tris 6.5, no salt
THPP[a]	$NiCl_2$	2.6 mM	4.8 mM	45% MPD, 0.1 M Tris pH 8.5, 0.2 M $MgCl_2$
THPP[a]	$CuCl_2$	3.0 mM	3.0 mM	25% PEG1500, 0.1 M Bis-Tris pH 6.5, 0.2 M AmA
THPP[a]	$ZnCl_2$	2.6 mM	5.0 mM	30% PEG400, 0.1 M HEPES pH 7.5, 0.2 M CaCl

[a] [THPP] = 10 mM

[b] Indicates monomer concentration

Table S5. Rosetta Interface Energy Calculations[a]

Structure	Trimer Energy (REU)	Monomer Energy (REU)	Trimer-Monomer Energy (REU)
Ni_2:[$^{A74/C96}$RIDC1]$_3$	-515.20	-539.44	24.25
Fe_2:[$^{A74/C96}$RIDC1]$_3$	221.29	246.37	-25.08

[a] Excludes energetic contribution of coordinating histidine residues and metal ions

Table S6. DFT-computed energies of metal coordination sites[a]

Protein	Coordination Site	Multiplicity	Overall Charge	Energy (B3LYP)[b],[c]
$^{A74/C96}$RIDC1^{red}	Fe^{II}:His_3	5	+2	-2093.28
$^{A74/C96}$RIDC1^{red}	Fe^{II}:His_5	5	+2	-2394.33
$^{A74/C96}$RIDC1^{red}	Fe^{II}:His_6	5	+2	-2620.57
$^{A74/C96}$RIDC1^{red}	Ni^{II}:His_3	3	+2	-2337.81
$^{A74/C96}$RIDC1^{red}	Ni^{II}:His_5	3	+2	-2638.86
$^{A74/C96}$RIDC1^{red}	Ni^{II}:His_6	3	+2	-2865.13
$^{A74/C96}$RIDC1^{red}	Ni^{II}:His_6 (alt. conf.)	3	+2	-2864.94

[a] Coordination sites extracted from crystal structures and without geometry optimization

[b] Energies reported in hartrees.

[c] 1 hartree = 627.50 kcal/mol

References

1. E. N. Salgado, X. I. Ambroggio, J. D. Brodin, R. A. Lewis, B. Kuhlman and F. A. Tezcan, *Proc Natl Acad Sci U S A*, 2010, **107**, 1827-1832.
2. H. Liu and J. H. Naismith, *BMC Biotechnol*, 2008, **8**, 91.
3. J. Faraone-Mennella, F. A. Tezcan, H. B. Gray and J. R. Winkler, *Biochemistry*, 2006, **45**, 10504-10511.
4. P. Schuck, *Biophys J*, 2000, **78**, 1606-1619.
5. J. Lebowitz, M. S. Lewis and P. Schuck, *Protein Sci*, 2002, **11**, 2067-2079.
6. N. Collaborative Computational Project, *Acta Crystallogr D Biol Crystallogr*, 1994, **50**, 760-763.
7. P. D. Adams, P. V. Afonine, G. Bunkoczi, V. B. Chen, I. W. Davis, N. Echols, J. J. Headd, L. W. Hung, G. J. Kapral, R. W. Grosse-Kunstleve, A. J. McCoy, N. W. Moriarty, R. Oeffner, R. J. Read, D. C. Richardson, J. S. Richardson, T. C. Terwilliger and P. H. Zwart, *Acta Crystallogr D Biol Crystallogr*, 2010, **66**, 213-221.
8. P. Emsley and K. Cowtan, *Acta Crystallogr D Biol Crystallogr*, 2004, **60**, 2126-2132.
9. E. Krissinel and K. Henrick, *J Mol Biol*, 2007, **372**, 774-797.
10. R. F. Alford, A. Leaver-Fay, J. R. Jeliazkov, M. J. O'Meara, F. P. DiMaio, H. Park, M. V. Shapovalov, P. D. Renfrew, V. K. Mulligan, K. Kappel, J. W. Labonte, M. S. Pacella, R. Bonneau, P. Bradley, R. L. Dunbrack, R. Das, D. Baker, B. Kuhlman, T. Kortemme and J. J. Gray, *J. Chem. Theory Comput.*, 2017, **13**, 3031-3048.
11. M. D. Hanwell, D. E. Curtis, D. C. Lonie, T. Vandermeersch, E. Zurek and G. R. Hutchison, *J Cheminform*, 2012, **4**, 17.
12. W. J. Hehre, *Accounts of Chemical Research*, 1976, **9**, 399-406.
13. M. V. Shapovalov and R. L. Dunbrack, Jr., *Structure*, 2011, **19**, 844-858.
14. C. Andreini, G. Cavallaro, S. Lorenzini and A. Rosato, *Nucleic Acids Res.*, 2013, **41**, D312-319.
15. E. N. Salgado, J. Faraone-Mennella and F. A. Tezcan, *J. Am. Chem. Soc.*, 2007, **129**, 13374-13375.
16. E. N. Salgado, X. I. Ambroggio, J. D. Brodin, R. A. Lewis, B. Kuhlman and F. A. Tezcan, *Proc. Natl. Acad. Sci. USA*, 2010, **107**, 1827-1832.